



<b>Title</b>	<b>Compression of micron-sized pillars of anodic aluminium oxide nano-honeycomb</b>
<b>Author(s)</b>	<b>Ng, KY; Lin, Y; Ngan, AHW</b>
<b>Citation</b>	<b>Journal Of The Mechanics And Physics Of Solids, 2011, v. 59 n. 2, p. 251-264</b>
<b>Issued Date</b>	<b>2011</b>
<b>URL</b>	<b><a href="http://hdl.handle.net/10722/134412">http://hdl.handle.net/10722/134412</a></b>
<b>Rights</b>	<b>NOTICE: this is the author's version of a work that was accepted for publication in Journal of the Mechanics and Physics of solids. Changes resulting from the publishing process, such as peer review, editing, corrections, structural formatting, and other quality control mechanisms may not be reflected in this document. Changes may have been made to this work since it was submitted for publication. A definitive version was subsequently published in Journal of the Mechanics and Physics of solids, 2011, v. 59 n. 2, p. 251-264. DOI: 10.1016/j.jmps.2010.10.008</b>

# **Compression of Micron-sized Pillars of Anodic Aluminium Oxide Nano-honeycomb**

K.Y. Ng, Y. Lin\*, and A.H.W. Ngan

Department of Mechanical Engineering, The University of Hong Kong, Pokfulam Road,  
Hong Kong, PR China

\* Correspondence Author (Email: ylin@hku.hk)

## **Abstract**

Micro-pillars of anodic aluminium oxide with nano-sized honeycomb channels along the pillar axis exhibit compressive stress-strain response with large excursions corresponding to discrete, inhomogeneous deformation events. Each excursion is found to associate with the severe distortion of a material layer at the pillar's head, whereas the remaining of the pillar remains intact. The stresses at which these excursions occur do not exhibit any significant dependence on the pillar size. A simple model is proposed to describe the response of pillars under compression, which energetically, as well as kinetically, explains as to why the localized deformation always takes place at the pillar head. Predictions on the occurrence of instability events from this model also quantitatively agree with the experimental observations.

**Keywords:** anodic aluminium oxide; micro pillars; plastic deformation; nanoindentation.

## 1. Introduction

Honeycomb structures have been well exploited in traditional engineering applications for their unique mechanical properties including large strength-to-weight ratio, high anisotropy, extended plastic plateau corresponding to strain localization, and so on [Chao et al. (1999), Chaung et al. (2002), Chen et al. (1999), Chuang et al. (2002), Gibson et al. (1989), Masters and Evans (1996), Ngan (2005a, 2005b), Onck et al. (2001), Simone and Gibson (1998), Triantafillou et al. (1989)]. The advent of nanotechnology has called for accelerated development and understanding of a broad range of nano-sized or nano-structured materials. Honeycomb structures with nano-sized pores are finding increasing applications as a result of their large surface area to volume ratio, and among these, anodic porous alumina (AAO) [Masuda et al. (1995, 1997a, 1997b)] is a relatively well-known nano-scale honeycomb material. Fig. 1 shows schematically the unique structure of AAO, which consists of vertically aligned nano-scale pore channels arranged in a closely packed pattern. AAO films are typically grown by anodizing on aluminium metal substrates. The pores in them are typically several tens of nanometres in diameter, and their length, which is also the thickness of the entire oxide film, can be made to be larger than 100  $\mu\text{m}$ , and so the aspect ratio of the channels is typically on the order of  $10^3$ . The solid AAO material forming the walls of the honeycomb channels is typically amorphous oxide, as revealed by X-ray diffraction (see later). Suggested applications of AAO include templating electrodes for supercapacitors [Chen et al. (2004)], catalytic microreactors for production of hydrogen from ammonia [Ganley et al. (2004)], membranes for high flow rate electroosmotic pumping [Vajandar et al. (2007)], environmental sensors [Varghese et al. (2003)], as well as host templates for the fabrication of other nano-structures including aligned carbon nanotube arrays [Hu et al. (2001)] and high-aspect-ratio nanowires of various materials [Rabin et al. (2003)], including zinc oxide [Li et al. (2000)], bismuth telluride [Sander et al. (2002)], antimony [Zhang et al. (2002)], and indium oxide [Zheng et al. (2001)].

Despite the many potential applications, the mechanical behaviour of AAO remains by and large unknown. In a recent paper [Ng et al. (2009)], we reported what

might be the first systematic study of the deformation microstructure of AAO honeycombs, under nanoindentation conditions. It was found that when indents are made on AAO along the channel axis, the load-displacement curve is decorated with rather periodic strain excursions, which are thought to be associated with an observed system of cracks which run perpendicular to the surface of the specimen underneath the indent. This system of cracks maintains a self similar pattern with respect to the size of the indent, and so as an indent is made progressively larger, the cracks will have to propagate sideways (i.e. along a direction perpendicular to the crack plane) in order to maintain self similarity with the indent size. In the subsurface direction, the deformation microstructure exhibits a very clear-cut elasto-plastic boundary, separating a heavily deformed zone adjacent to the contact with the indenter, from a zone which has undergone no apparent plastic deformation. The cracks mentioned above reside inside the heavily deformed zone, as boundaries separating a fully compacted zone of the AAO material nearer to the indent centre, from another zone in which the AAO structure is only mildly tilted. This mode of deformation appears to be unique, and its “all-or-none” nature (i.e. either heavily deformed or otherwise remains apparently elastic) suggests that AAO might be an excellent strain isolation material for cushioning mechanical impact, possibly in micro-machinery applications.

Whereas our previous study concerns indentation on AAO in a near half-space morphology (“near” because the AAO film is supported by aluminium substrate), another testing protocol which has become increasingly popular is compression of micron-sized pillars [Uchic et al. (2004)]. Micro-pillars of face-centred-cubic metals, including Ni and Ni<sub>3</sub>Al [Uchic et al. (2004), Dimiduk et al. (2005)], Au [Greer et al. (2005)] and Al [Ng and Ngan (2008)], reveal a strong size dependence of yield strength, with jerky and stochastic deformation behaviour. In this paper, we report a study on the compressive response of micro-pillars of AAO. Comparing to indentation on a specimen occupying a half space, the stress state in a pillar undergoing uniaxial compression is a lot simpler, and therefore the interpretation of results is much more straightforward. Also, in the light of the already large volume of literature on micro-pillars of other materials, a similar study on AAO with a unique channel structure should provide an interesting comparison.

## 2. Experimental

Aluminium discs of 1 inch diameter were cut out from a 300 $\mu\text{m}$ -thick, 99.999% pure Al sheet by electrical discharge machining. The prepared discs were annealed in a vacuum better than  $10^{-7}$  torr at 550 $^{\circ}\text{C}$  for two days to allow grain growth to occur. The surfaces of the Al discs were pre-treated mechanically and then subsequently electropolished in 20% perchloric acid in methanol to obtain a residual-stress-free surface with smoothness of about 1 $\mu\text{m}$ , which is suitable for the later anodization steps. Nanoporous AAO structures were then prepared by anodic oxidation of the pre-treated Al discs in a 0.3M oxalic acid solution at 40V DC in a constant temperature environment of  $(17 \pm 0.1)^{\circ}\text{C}$ , achieved using an electronic feed-back controlled water bath. Since the structure of the resultant AAO film is well known to be very sensitive to the anodization environment, to obtain highly ordered AAO nano-honeycomb structure, a 2-step anodization method as first described by Masuda et al, (1995, 1997a) was employed. The first anodization step involved forming an initial layer of AAO on the Al substrate by performing anodic oxidation in the above conditions for 6-10 hrs. This initial layer was then removed by a phosphochromic acid solution (1.5wt%  $\text{H}_2\text{CrO}_4$  in 6wt%  $\text{H}_3\text{PO}_4$ ), followed by performing a second anodization step on the now anodic-oxide free Al substrates at the same anodizing conditions for another 10hrs to form a better AAO layer. The structure of the prepared anodic oxide films was revealed by X-ray diffraction in a Siemens Bruker AXS D8 Advance X-ray diffractometer, as well as by electron diffraction in a Tecnai 20 transmission electron microscope (TEM).

Micro-pillars of AAO were then prepared on an AAO film grown on top of the same underlying Al grain by a Quanta 3D Focused Ion Beam (FIB) system. Pillars were milled on top of the same underlying Al grain to ensure homogeneity and consistency, since AAO film grown on top of the same grain has a very homogenous quality. Five groups of micro-pillars of diameters ranging from 700nm, 1 $\mu\text{m}$ , 2 $\mu\text{m}$ , 2.4 $\mu\text{m}$  to 2.8 $\mu\text{m}$  were prepared with an aspect ratio typically from 1:2 to 1:3 to avoid bending fracture during compression. Uniaxial compression tests were carried out in a Hysitron

Triboscope Nanoindenter with a flat-ended punch installed. All the tests were carried out in the ambient environment and the morphology of the columns before and after compression was examined and compared using a LEO 1530 FEG scanning electron microscope (SEM). The raw load-displacement data from the compression tests were converted to nominal stress and strain data by normalizing load and displacement with the SEM-measured cross-sectional area and height of the pillar respectively. The data presented below have been thermal-drift corrected, by measuring the displacement change during a low-load holding step of typically about 1 minute incorporated in the load profile. In this low-load holding step, any displacement change against time was recorded, and the raw displacement data during the whole test was offset by this measured displacement rate to remove any thermal effect due to ambient environment changes.

### 3. Results

The subfigures alongside the schematic in Fig. 1 show the real SEM morphology of the AAO prepared in the present study. It can be seen that the pore channels are closely packed together forming a hexagonal honeycomb structure. These pores were round in shape with a diameter of about 70nm, and on average there were  $5 \times 10^{13}$  pores per  $m^2$  of the film surface. As illustrated in the cross sectional SEM micrograph in Fig. 1, these planar pores were parallel aligned tubular channels which, after 10 h of electrochemical oxidation in the second-step-anodization, extended from the film surface to the Al substrate in the normal direction. The AAO film on which the micro-pillars were produced by FIB was measured to be about 100  $\mu m$  in thickness, which is more than ~30 times the height of the micro-pillars made subsequently.

Fig. 2(a) shows the X-ray diffraction (XRD) result of the fabricated AAO film. Over the entire scanning range, no distinctive peak belonging to crystalline aluminium oxide was found, implying that the structure of the AAO was amorphous in nature. At diffraction angle of around  $44.7^\circ$ , a sharp peak corresponding to the Al (200) reflection was observed in the scanning spectrum, and this is likely to originate from the highly

textured aluminium substrate after subsequent annealing in the pre-treatment steps. Selective area diffraction (SAD) in the TEM performed on a longitudinal section of the AAO film prepared by FIB, as shown in Fig. 2(b), confirms that the AAO structure was amorphous.

Fig. 3(a)-(c) show the morphology of the 1 $\mu$ m AAO micro-column before and after the compression test. It can be seen that deformation happened predominantly at the head of the column, but not at the other parts of the pillar. Similar observation was found in all sizes of the pillars being tested. Examination at a higher magnification (Fig. 3 (c)) shows that the deformed region at the pillar's head is in fact a severely distorted layer distinctively different from the remaining part of the pillar which shows no discernible sign of deformation. In the experiments such as that shown in Fig. 3, the deformation was stopped at a maximum strain of about 30%. Going beyond this value could result in sudden fracture of the pillar, as shown in the example described in Fig. 4, where the pillar fractured at a strain of about 30%.

Fig. 5 shows the typical stress-strain behaviour during the compression of the columns of 1 $\mu$ m in diameter, to a maximum strain of about 30%. All these data were thermal drift corrected, as explained in Section 2. It can be seen that the overall deformation process was not smooth but was accompanied by a few large excursions or plateaus with sizes ranging from 50nm to 200nm. At relatively lower stresses, the stress-strain response appeared to be linear, but when the applied stress exceeded 17.5GPa, a series of excursions occurred. Careful inspection of individual stress-strain curves reveals that they are all linear when the applied stress was below a value of about 17.5GPa, irrespective of the diameter of the micro-pillars. It is noted that the linear region of the pillars was rather repeatable in all groups of pillars tested, as shown in Fig. 5(b)-(f). The Young modulus of this linear region was measured to be  $31.2 \pm 3.7$  GPa,  $43.1 \pm 3.1$  GPa,  $47.7 \pm 4.5$  GPa,  $46.2 \pm 5.4$  GPa, and  $46.6 \pm 10.8$  GPa, for pillar diameter of 700nm, 1 $\mu$ m, 2 $\mu$ m, 2.4 $\mu$ m and 2.8 $\mu$ m respectively. Considering the scatter of the results, there is no apparent trend of the Young modulus with the pillar diameter in the range studied. The inset of Fig. 5(a) shows a plot of the first yield stress, i.e. the stress at which the first

excursion occurs, versus the sample size. It can be seen that there is again no statistically significant change in the first yield strength with sample size.

After the first excursion, subsequent excursions may occur in the stress-strain curve, and these were rather large typically about  $100 \pm 50\text{nm}$  in size. In general 2 to 3 excursions in total could occur in a single pillar before fracture. In some pillars of lower aspect ratio such as the set of 700nm diameter, it appears that further excursions could happen if the tests were not stopped. To provide better understanding of these excursions, the onset of the first three excursions are plotted in Fig. 6. Here, the pillar sizes are demarcated by different symbols, and the orders of the excursions are demarcated by the different colours of the symbols. It can be seen that the data for the first excursion in different sizes of pillars are more crowded together, whereas those for the second and third excursions appear to be more scattered, probably due to the deformed shape of the column once the first excursion has occurred, which introduces complexities for further deformation. The sizes of the excursions are plotted in Fig. 7. In most cases, the average size of the excursions is around 100nm with a standard deviation of typically 50-100nm, but in some odd cases the excursion size could reach about  $1\mu\text{m}$ . The SEM of these large excursions, shown in the inset of Fig.7, suggests that the highly deformed layer has apparently slid to one side of the pillar head, possibly due to an angular misalignment between the pillar head and the compression punch.

In order to study the microstructural evolution during formation of sequential excursions, some compression tests were interrupted immediately after the first excursion, and others were interrupted after the third excursion. As shown in Fig. 8, the pillar with only one excursion (curve B) apparently exhibited one distinctive deformed layer at its head, whereas the other column with three excursions (curve A) showed three severely deformed layers, as indicated by arrows in the inset. This suggests that each excursion in the stress-strain curve is likely to be associated with the distortion of one layer of AAO material at the top of the pillar.

#### **4. Discussions and a simple mechanics model**



It has been reported that the strength of crystalline materials in general demonstrates a significant increase, typically up to several times in magnitude, when the sample size is in miniature scale [Uchic et al. (2004), Dimiduk et al. (2005), Greer et al. (2005), Ng and Ngan (2008)] An explanation for such size dependence of strength is mainly due to the fact that the characteristic length scale governing dislocation processes, such as multiplication, is much more limited in miniature sized samples than in bulk ones [Parthasarathy et al. (2007)]. Materials in which dislocations do not exist, such as metallic glasses, deform by the formation and propagation of highly localized shear bands [Schuster et al. (2007), Volkert et al. (2008)], and in such cases reduction of sample size does not affect the yield strength in any significant way. The present results on AAO micro-pillars (Fig. 6) suggest that there is no significant size dependence of the yield strength, and so the behaviour is similar to other amorphous materials studied [Schuster et al. (2007), Volkert et al. (2008)]

The more interesting finding from the present AAO micro-pillars, however, is the development of a highly deformed layer at the pillar's head, and this, as suggested by the results in Fig. 8, is likely to be associated to an excursion in the stress-strain curve. Apart from this distorted layer, the remaining of the pillar does not show discernible deformation. This "all-or-none" mode of deformation of the AAO structure along its channel axis, i.e. either heavily deformed or not at all, was also observed during nanoindentation on AAO in a half-space morphology [Ng et al. (2009)]. In the present experiments involving micro-pillars, after the first excursion, multiple sequential excursions can happen. Interestingly, if the aspect ratio is low enough to avoid bending fracture, extra excursions could occur until the entire sample length vanishes, as is apparent in the 700nm pillar in Fig. 9, which exhibited excursions up to a strain of 80%. However, large plastic strains were not observed in pillars with higher aspect ratios, which fractured already at moderate strains.

The formation of the highly distorted layer at the pillar's head is likely to be due to the pore channels in AAO which provide a highly compressible structure to enable

severe distortion. Here, a simple mechanics model is presented which aims to provide some salient features of the AAO deformation. Consider an AAO pillar with length  $L$  being compressed along the axial direction of the honeycomb, as shown in Fig. 10. To accommodate a compression  $\delta$ , assume that the pillar can either undergo entirely elastic deformation, as depicted in Fig. 10(b), or deform in an inhomogeneous manner such that a top part of the sample, with length  $z$ , tilts with an angle  $\theta$  as shown in Fig. 10(c). We must point out that the deformation mode shown in Fig. 10(c) has indeed been observed during actual compression test, see Fig. 7 and Fig. 8 for example. For the configuration in Fig. 10(c), the tilted zone is considered to form at the top part, instead of at mid-length, of the sample because only one kink interface is involved for a tilted zone at the top part, while two kink planes must exist to form a tilted zone at mid-length. The tilting may be opposed by the friction between the compression punch and the sample's head, and this effect will be considered later. To determine which configuration in Fig. 10 is more likely to occur, we need first to examine the amount of energy needed to be input to drive such deformations. For the elastic deformation as shown in Fig. 10(b), the strain and the total energy stored in the pillar (per unit cross-sectional area) are

$$\varepsilon_0 = \frac{\delta}{L} ; \quad W_0 = \frac{1}{2} E \varepsilon_0^2 L = \frac{E \delta^2}{2L} \quad (1)$$

where  $E$  is the Young's modulus of AAO in the axial direction. On the other hand, to cause a deformation as shown in Fig. 10(c), the total work needed to be done is

$$W = W_e + W_t \quad (2)$$

in which  $W_e$  is the energy stored in the elastic part, with length  $L - z$ , of the pillar and  $W_t$  is the amount of energy dissipated in the tilted part. In other words, here it is assumed that elastic deformation is negligible in the tilted part which we believe is reasonable given the fact that most plastic deformation is localized within this thin region whose size is small compared to the whole pillar. It is easy to verify that the stress in the elastic part of the sample takes the form

$$\sigma_e = E \frac{\delta - z[1 - \cos(\theta)]}{L - z} \quad (3)$$

where the numerator represents the net compression acting on the untilted part, with length  $L - z$ , of the specimen which is assumed to behave elastically.  $W_e$  can then be calculated as

$$W_e = E \frac{\{\delta - z[1 - \cos(\theta)]\}^2}{2(L - z)} \quad (4)$$

The deformation shown in Fig. 10(c) must involve the kinking of longitudinal periodic units of AAO, as well as the relative sliding among them [Ng et al. (2009)]. Assume the kinking of periodic units of AAO takes place over a small segment, with length  $s$ , as shown in Fig. 11(a), then the moment  $M$ , as a function of kink angle  $\theta$ , necessarily to be applied on this segment is schematically plotted in Fig. 11(b). Basically, we expect the periodic unit to behave elastically at the beginning, then as the angle  $\theta$  increases the response becomes totally plastic and the moment  $M$ , in this case, reaches a constant value  $M_0$ . If plastic deformation is assumed to be dominant during kinking, then  $W_t$  is expected to take the form

$$W_t = M_0 \theta + \tau_c z \tan \theta \quad (5)$$

where the second term on the right hand side corresponds to the dissipated work caused by the sliding among periodic units of AAO, which are assumed to possess a constant frictional stress  $\tau_c$  against sliding, as discussed in [Ng et al. (2009)]. It should be noted that, for the sake of dimensional consistency,  $M_0$  in Eq. (5) is the resisting moment per unit area corresponding to the bend in the structure. Although the functional form in Eq. (5) is empirical, it is believed to be a satisfactory representation because the divergence of

the  $\tan\theta$  term for large values of  $\theta$  tallies with the expected rapid rise in energy as the AAO structure becomes densely compacted at large deformation.

We proceed by analyzing the maximum stress the tilted part can support. As illustrated in Fig. 12(a), assume a normal stress  $\sigma$  is acting on the top and bottom face of the tilted region with height  $h = z \cos \theta$ . For any given  $z$ , at equilibrium the work done by external loading during an infinitesimal change in  $h$  must be balanced by the amount of energy dissipated in the tilted region, which, in the light of Eq. (5), leads to

$$\sigma_t = -\frac{\partial W_t}{\partial h} = \frac{1}{z \sin \theta} \left[ M_0 + \tau_c z \frac{1}{\cos^2 \theta} \right] \quad (6)$$

where  $\sigma_t$  should be interpreted as the maximum normal stress the tilted part can sustain without further deformation. Note that the residual stress, given in Eq. (3), in the elastic part of pillar after tilting must also be shared by the tilted part, hence at equilibrium we have

$$\sigma_t = \sigma_e. \quad (7)$$

For given values of  $\delta$  and  $z$ ,  $\sigma_t$  and  $\sigma_e$  as functions of tilting angle  $\theta$  are schematically shown in Fig. 13. Notice that  $\sigma_t$  is singular at  $\theta = 0$ , see Eq. (6), so typically there are two intersection points between the curves representing  $\sigma_t$  and  $\sigma_e$  which we refer to as  $\theta_{cr}$  and  $\theta_{eq}$  as shown in Fig. 13.  $\sigma_e$  is larger than  $\sigma_t$  only in the region  $\theta_{cr} < \theta < \theta_{eq}$  – physically, this means that spontaneous tilting will not happen until the angle reaches  $\theta_{cr}$ , this critical angle also sets the condition for the onset of tilting. Once the tilting angle passes  $\theta_{cr}$  by some nucleation mechanisms, the residual stress in the pillar becomes large enough to drive further deformation. The tilting will finally stop when the angle reaches  $\theta_{eq}$ , which is the stable equilibrium position of the system. Hence, the two variables  $z$  and  $\theta$  are not independent, but instead, the final tilting angle  $\theta$  relates to  $z$  through Eq. (7). In addition, we expect the equilibrium configuration to be such that the total amount of

work needed to be done in driving the deformation as shown in Fig. 10(c) is minimized, that is

$$\frac{dW}{dz} = \frac{d}{dz} \left\{ \frac{E[\delta - z(1 - \cos(\theta))]^2}{2(L - z)} + M_0\theta + \tau_c z \tan \theta \right\} = 0 \quad (8)$$

which provides us the condition for the determination of  $z$ . Choosing  $\tau_c / E = 0.91 \times 10^{-2}$  and  $M_0 / EL = 3 \times 10^{-4}$ ,  $W$  as functions of  $z$  under different compression depths are shown in Fig. 14. Clearly, in all cases,  $W$  takes the minimum at certain moderate  $z$  value. Another important feature demonstrated by Fig. 14 is that the ratio between this minimum value of  $W$  and  $W_0$  defined in Eq. (1) varies as the compression depth  $\delta$  increases. Basically, this ratio is larger than 1 when  $\delta$  is small and then becomes less than one as  $\delta$  increases. This observation is important because from the energetic point of view, tilting is expected to happen only when  $W$  is less than  $W_0$ . Hence, the critical compression depth  $\delta_1$  beyond which the tilting deformation as shown in Fig. 10(c) is more favourable to take place can be determined by

$$W(\delta_1) = W_0(\delta_1) = \frac{E\delta_1^2}{2L}. \quad (9)$$

Note also that the instability at  $\delta_1$  ( $= 0.055L$  in Fig. 14) happens at a critical  $z$  ( $= 1.45\delta = 0.08L$  in Fig. 14). This means that, referring to Fig. 10(c), a fixed length of the pillar's top part suddenly collapses at the critical point – this is an interesting variant of buckling with a well-defined plastic region. Also, given that the critical  $z = 0.08L$ , the tilted zone's residual thickness  $h = z \cos \theta$  is predicted to be on the order of a few percent of  $L$ . The pillars in Fig. 8 were 2 to 3 microns long, and their deformed layers are estimated to be 100 to 200nm thick, and so broad agreement exists with the theoretical prediction.

The deformation diagram of the pillar is schematically illustrated in Fig. 15, initially when the strain is small, the whole sample deforms elastically and the stress

increases linearly with strain. However, as the strain reaches the critical value  $\varepsilon_1 = \delta_1 / L$ , the tilted deformation becomes energetically more favourable and a sudden transition from the configuration shown in Fig. 10(b) to that in Fig. 10(c) will take place. As a result of this instability event, a certain amount of elastic strain is released and the stress level in the pillar undergoes a sudden drop at  $\varepsilon_1$ , see Fig. 15. Upon further continuous straining beyond  $\varepsilon_1$ , the kink band formed may tilt further (i.e.  $\theta$  increasing) continuously, but within our model, it may not expand downward along  $z$  in a continuous fashion. To propagate the kink band continuously along  $z$  would mean that for an infinitesimal increment in the overall compression  $d\delta$ , a new layer with an infinitesimal thickness  $dz$  immediately below the kink band would join it. This new layer  $dz$  is originally elastic as the rest of the material of length  $(L-z-dz)$  below the kink band, and so the question is whether the elastic energy stored in the length  $(L-z)$  immediately after the formation of the first kink band (of untilted length  $z$ ) could drive this length to kink over a thickness of  $dz$ , which would then join the already formed kink band. The answer is negative, because the energy expended in forming a new kink of length  $dz$ , from Eqn. (5), would be  $W_t = 2M_0\theta + \tau_c dz \tan \theta$  (the first term on the right hand side is doubled since work must be done to bend the material on the two walls of the kink) which tends to a finite value  $2M_0\theta$  as  $dz$  tends to zero. Such a finite amount of energy cannot be supplied by the infinitesimal increase in elastic strain energy during an infinitesimal increment  $d\delta$  in compression, and so instead of the old kink band thickening by  $dz$ , the column  $(L-z)$  below would simply deform elastically in a homogeneous manner. The assumption here is that the microstructural damage adjacent to the interface of the already formed kink band does not significantly reduce the energy dissipation required to thicken it from what is given in Eqn. (5), i.e. any heterogeneous nucleation factor is ignored here. Within this assumption, the kink band formed in the first instability event in Fig. 15 therefore does not propagate continuously on increasing compression, and in fact, the present experimental results provided no evidence for such continuous propagation of kink bands. However, as compression keeps increasing, the stress in the elastic part of the sample  $(L-z)$  can be sufficiently recovered to fulfil the condition in Eqn. (9) (albeit replacing  $L$  by  $(L-z)$ ), and so a new kink band will be triggered. The length of this kink band, however, is

not an infinitesimal value  $dz$ , but is a finite value determined by the condition in Eqn. (9), when the elastic energy stored is just enough to drive the kinking. This new kink band is likely to form just next to the first kink band as shown in Fig. 15, because the material structure in the kink plane of the latter should be sufficiently weakened and so the formation of a new band on this interface should be energetically more favourable. The tilting of the second band is also likely to be in opposite direction to the first in order to offset the sideways motion of the pillar's top. In other words, as straining proceeds, a series of discrete kink bands are expected to form in succession as in Fig. 15. Although the previously formed bands may tilt further, they do not thicken, and new ones formed in a discrete manner on continuous compression.

If the compression is load controlled instead of displacement controlled as discussed above, then, instead of load drops, the instability events are represented by displacement excursions as shown by the dashed line in Fig. 15. The comparison between model predictions and experiment data is shown in Fig. 16, where the material parameters are chosen as  $E = 38\text{GPa}$ ,  $\tau_c / E = 0.91 \times 10^{-2}$  and  $M_0 / EL = 3 \times 10^{-4}$ . We want to re-emphasize that, in predicting the second instability event, the pillar length should be treated as  $L - z$ , with  $z$  being the length of the first tilted layer. In addition, in this case a new kink plane is formed, and the first kink plane now becomes the interface between the first and the second tilted zone (see the third diagram in Fig. 15) which also dissipates energy. As a crude approximation to represent these, the first term on the right hand side of Eq. (5) is modified to  $2M_0 \theta$ . As shown in Fig. 16, our model captures very well the key features of the experiment observations, such as the right critical stress, as well as strain, for the first two instability events. Notice that the porous nature of AAO should make the sliding of its periodic units relatively easy, hence  $\tau_c$  is expected to be much smaller than  $E$ . In addition, since pillar length  $L$  is much larger than the pore size, we expect the ratio between  $M_0$  and  $EL$  to be very small. These two observations suggest that the parameters we are choosing in the calculation, i.e.  $\tau_c / E = 0.91 \times 10^{-2}$  and  $M_0 / EL = 3 \times 10^{-4}$ , are not unreasonable.

Until this point, our discussions have been focusing on the energetic aspect of the problem. However, as illustrated in Fig.13, the tilting angle must reach a critical value  $\theta_{cr}$  before the stress field in the elastic domain is large enough to drive the tilted deformation. In other words, despite being energetically more favourable, tilting may not be able to take place because kinetically this critical angle is just too large for any possible nucleation mechanism to achieve. Note that these conclusions are obtained under the assumption that the tilted layer is subjected to normal stress only, as shown in Fig. 12(a). What if there are shear stresses acting on the pillar as well? To investigate this, assume a friction-induced shear stress  $\mu\sigma$  is acting on the top, as well as the bottom, of the tilted region as shown in Fig. 12(b). Following the same arguments as before, we have

$$\sigma_t = \frac{1}{z(\sin\theta + \mu\cos\theta)} \left[ M_0 + \tau_c z \frac{1}{\cos^2\theta} \right] \quad (10)$$

Comparing Eq. (10) to (6), it is clear that the singularity of  $\sigma_t$  at  $\theta=0$  has been eliminated by the presence of friction. To see the important consequences of this,  $\sigma_t$  as functions of  $\theta$  for different  $\mu$  values are plotted in Fig. 17. Here the parameters are chosen as identical to those in Fig. 16, and  $\delta$  is taken to be 0.055 which is the critical compression depth for the first instability event as shown in Fig. 16.

From Fig. 17, it is obvious that increasing in the friction coefficient  $\mu$  leads to a decrease in the critical angle  $\theta_{cr}$  for the onset of spontaneous tilting. Furthermore, when friction is large enough, for example as  $\mu = 0.3$ , this critical angle no longer exists and spontaneous tilting is expected to happen even when the periodic units of AAO are perfectly aligned, i.e.  $\theta = 0$ .

We believe this finding has deeper implications in understanding several important experiment observations. First of all, it may provide a kinetic explanation for the question as to why the pillar always tilts first at the top. Energetically, as mentioned



before, we know the first tilted layer should be formed at the top because in this case only one kink plane needs to be created, see Fig. 10(c), whereas the formation of a tilting region in the middle of the pillar requires two kink planes. Kinetically, we can understand this phenomenon by realizing that, in reality, the slight tapering of the micro-pillar geometry due to specimen drift during the FIB process may give rise to a small elevation of stress near the top. Also, a high shear stress can be generated locally at the top of pillar due to surface asperities, however, such perturbation in shear stress is likely to be homogenized, that is, the peak shear stress value decays rapidly, as one moves away from the top. These may explain why tilting is most likely to be nucleated at the top of the sample. Secondly, the important role of shear stress in the tilting process also suggests that the experiment results must be sensitive to factors like the roughness of the pillar surface and the possible mis-alignment between the indenter and the sample, which, we believe, provides a reasonable explanation for the spreading of data from experiment to experiment.

## Conclusions

Compression experiments on micro-pillars of AAO along the pore channel direction indicate that these micro-pillars deform in a highly inhomogeneous manner, involving the formation of a heavily distorted region at the pillar's head, whereas the remaining of the pillar remains intact. The stress-strain response exhibits excursions each of which corresponds to the severe distortion of a layer of the AAO structure at the pillar's head. The stresses at which these excursions occur do not show any significant dependence on the pillar size. A mechanics model is proposed to describe the deformation of AAO pillars under compression which seems to have captured all the essential features observed in experiment. The present results demonstrate the promising potential of using AAO as a sacrificial shielding material for thin film sensors or the supporting materials against mechanical damage, in applications involving mechanical contact with other components.

It will be interesting to know how such AAO nano-honeycombs behave under high strain rate loading, a condition commonly encountered in, for example, dynamic impact applications. However, this issue is beyond the scope of this paper and is left for future investigations. Modelling of porous materials has always been a challenge due to the complicated geometry. Nonetheless, we believe that the model presented here, although simple, may have shed light on the actual deformation mechanism of AAO, and thus can be served as a basis for more comprehensive studies in the future.

### **Acknowledgments**

The work described in this paper was supported by grants from the Research Grants Council (Project No. HKU7156/08E), as well as from the University Grants Committee (Project No. SEG-HKU06) of the Hong Kong Special Administration Region, P.R. China.

**Figure captions:**

- Fig.1 Schematic and real SEM micrographs of anodic aluminium oxide nano-honeycomb in top, cross sectional and bottom view. The bottom view is achieved by removing the aluminium substrate.
- Fig.2 (a) X-ray diffraction spectrum, (b) TEM image of a longitudinal section of the AAO with electron diffraction pattern as inset.
- Fig.3 SEM micrograph showing the original morphology of micro-columns (a) before the compression tests and (b) after the compression and (c) at higher magnification, it can be seen that deformation happened at the head of the column, forming a compact layer on top of the column. The column in the micrograph was  $1\mu\text{m}$  in diameter.
- Fig.4 SEM micrograph showing a fractured  $1\mu\text{m}$  column when the nominal strain exceeded 30%. Inset: the corresponding stress-strain response of during the compression test.
- Fig.5 (a) Typical compressive behaviour of  $1\mu\text{m}$  diameter pillars. Excursions are commonly observed after the yield point in the stress-strain curves. Inset: Yield strength versus pillar diameter. (b-f) Stress-strain response of 700nm columns (b),  $1\mu\text{m}$  columns (c),  $2\mu\text{m}$  columns (d),  $2.4\mu\text{m}$  columns (e), and  $2.8\mu\text{m}$  columns (f).
- Fig.6 Scatter plot showing the onset of the first three excursions of the five sets of column samples
- Fig.7 The size of the first three excursions of the five sets of column samples in the investigation. (hollow: the first excursion; solid-filled: the second excursion and half-filled the third excursion) Inset: SEM micrograph showing the deformed compact structure slide over the underneath column of the deformed  $2\mu\text{m}$  pillar.
- Fig.8 SEM micrographs showing the morphology of the compressed column after given out one excursion (curve B) and three excursions (curve A) in the stress-strain curves. The columns were  $1\mu\text{m}$  in diameter.
- Fig.9 Comparison of stress-strain response of a  $1\mu\text{m}$  column and a 700nm column. The  $1\mu\text{m}$  column fractured at around 30% strain, whereas the

700nm column exhibited excursions up to 80% strain without noticeable fracture.

- Fig. 10 Schematic plot of possible deformation configurations of an AAO pillar subjected to compression.
- Fig. 11 (a) Illustration of the kinking of periodic unit of AAO; (b) Schematic plot of the moment, necessary for tilting, as a function of the tilting angle.
- Fig. 12 Diagram of a tilted volume element subjected to normal stress (a); normal and shear stress (b).
- Fig. 13 Schematic plot of  $\sigma_t$  and  $\sigma_e$  as functions of tilting angle  $\theta$ .
- Fig. 14  $W$  as functions of  $z$  under different compression depths.
- Fig. 15 Schematic plot of the stress-strain relationship of AAO pillars under compression.
- Fig. 16 Comparison between model predictions and experiment data.
- Fig. 17  $\sigma_t$  and  $\sigma_e$  as functions of tilting angle  $\theta$  (in radians).

## References

- [1] Chao, L.P., Huang, J.H., Huang, Y.S., 1999. The influence of aspect ratio of voids on the effective elastic moduli of foamed metals. *Journal of Composite Materials* 33 (21), 2002-2016.
- [2] Chaung, C.H., Huang, J.S., 2002. Yield surfaces for hexagonal honeycombs with plateau borders under in-plane biaxial loads. *Acta Mechanica* 159 (1-4), 157-172.
- [3] Chen, C., Lu, T.J., Fleck, N.A., 1999. Effect of imperfections on the yielding of two-dimensional foams. *Journal of the Mechanics and Physics of Solids* 47 (11), 2235-2272.
- [4] Chen, Q.L., Xue, K.H., Shen, W., Tao, F.F., Yin, S.Y., Xu, W., 2004. Fabrication and electrochemical properties of carbon nanotube array electrode for supercapacitors. *Electrochimica Acta* 49 (24), 4157-4161.
- [5] Chuang, C.H., Huang, J.S., 2002. Elastic moduli and plastic collapse strength of hexagonal honeycombs with plateau borders. *International Journal of Mechanical Sciences* 44 (9), 1827-1844.
- [6] Dimiduk, D.M., Uchic, M.D., Parthasarathy, T.A., 2005. Size-affected single-slip behavior of pure nickel microcrystals. *Acta Materialia* 53 (15), 4065-4077.
- [7] Ganley, J.C., Seebauer, E.G., Masel, R.I., 2004. Porous anodic alumina microreactors for production of hydrogen from ammonia. *Aiche Journal* 50 (4), 829-834.
- [8] Gibson, L.J., Ashby, M.F., Zhang, J., Triantafillou, T.C., 1989. Failure Surfaces for Cellular Materials under Multiaxial Loads .1. Modeling. *International Journal of Mechanical Sciences* 31 (9), 635-663.
- [9] Greer, J.R., Oliver, W.C., Nix, W.D., 2005. Size dependence of mechanical properties of gold at the micron scale in the absence of strain gradients. *Acta Materialia* 53 (6), 1821-1830.
- [10] Hu, W.C., Gong, D.W., Chen, Z., Yuan, L.M., Saito, K., Grimes, C.A., Kichambare, P., 2001. Growth of well-aligned carbon nanotube arrays on silicon substrates using porous alumina film as a nanotemplate. *Applied Physics Letters* 79 (19), 3083-3085.

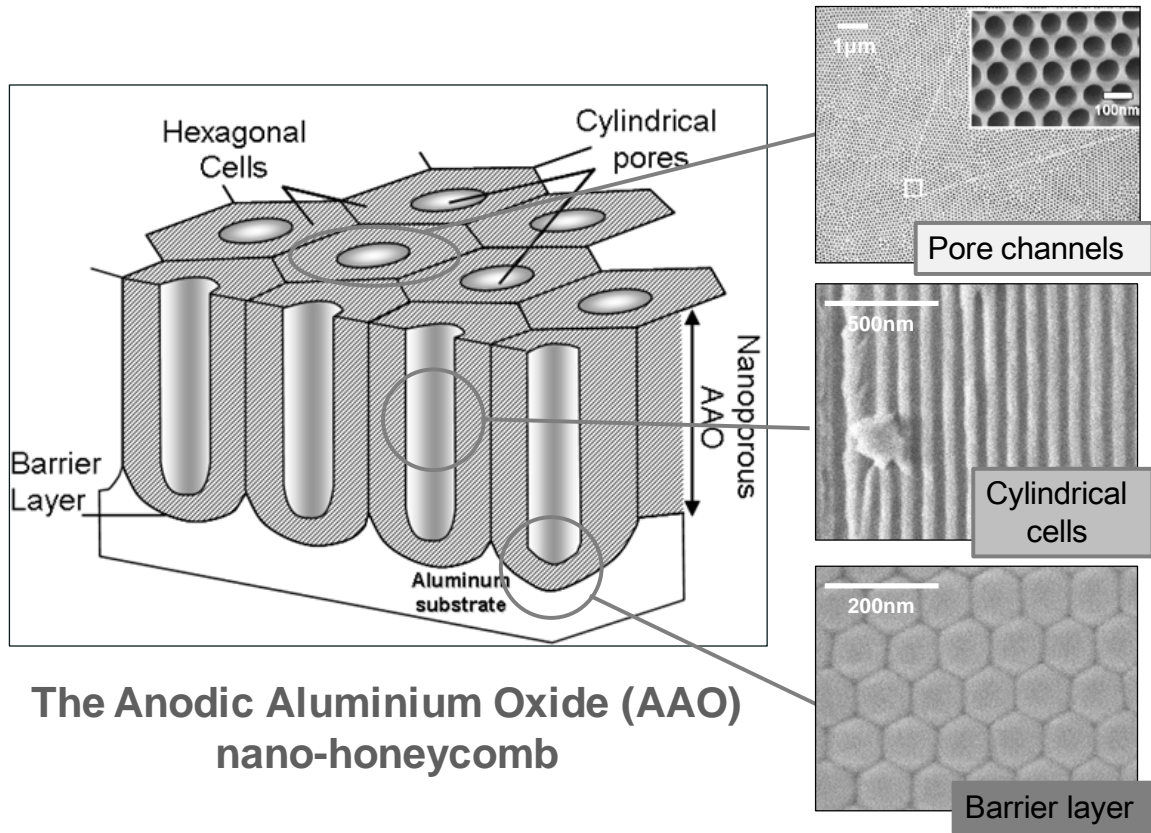
- [11] Li, Y., Cheng, G.S., Zhang, L.D., 2000. Fabrication of highly ordered ZnO nanowire arrays in anodic alumina membranes. *Journal of Materials Research* 15 (11), 2305-2308.
- [12] Masters, I.G., Evans, K.E., 1996. Models for the elastic deformation of honeycombs. *Composite Structures* 35 (4), 403-422.
- [13] Masuda, H., Fukuda, K., 1995. Ordered Metal Nanohole Arrays Made by a 2-Step Replication of Honeycomb Structures of Anodic Alumina. *Science* 268 (5216), 1466-1468.
- [14] Masuda, H., Hasegawa, F., Ono, S., 1997. Self-ordering of cell arrangement of anodic porous alumina formed in sulfuric acid solution. *Journal of the Electrochemical Society* 144 (5), L127-L130.
- [15] Masuda, H., Yamada, H., Satoh, M., Asoh, H., Nakao, M., Tamamura, T., 1997. Highly ordered nanochannel-array architecture in anodic alumina. *Applied Physics Letters* 71 (19), 2770-2772.
- [16] Ng, K.S., Ngan, A.H.W., 2008. Stochastic nature of plasticity of aluminum micro-pillars. *Acta Materialia* 56 (8), 1712-1720.
- [17] Ng, K.Y., Lin, Y., Ngan, A.H.W., 2009. Deformation of anodic aluminum oxide nano-honeycombs during nanoindentation. *Acta Materialia* 57 (9), 2710-2720.
- [18] Ngan, A.H.W., 2005. On the distribution of elastic forces in disordered structures and materials. I Computer simulation. *Proceedings of the Royal Society of London Series a-Mathematical Physical and Engineering Sciences* 461 (2054), 433-458.
- [19] Ngan, A.H.W., 2005. On the distribution of elastic forces in disordered structures and materials. II - A statistical mechanics theory. *Proceedings of the Royal Society a-Mathematical Physical and Engineering Sciences* 461 (2057), 1423-1446.
- [20] Onck, P.R., Andrews, E.W., Gibson, L.J., 2001. Size effects in ductile cellular solids. Part I: modeling. *International Journal of Mechanical Sciences* 43 (3), 681-699.

- [21] Parthasarathy, T.A., Rao, S.I., Dimiduk, D.M., Uchic, M.D., Trinkle, D.R., 2007. Contribution to size effect of yield strength from the stochastics of dislocation source lengths in finite samples. *Scripta Materialia* 56 (4), 313-316.
- [22] Rabin, O., Herz, P.R., Lin, Y.M., Akinwande, A.I., Cronin, S.B., Dresselhaus, M.S., 2003. Formation of thick porous anodic alumina films and nanowire arrays on silicon wafers and glass. *Advanced Functional Materials* 13 (8), 631-638.
- [23] Sander, M.S., Prieto, A.L., Gronsky, R., Sands, T., Stacy, A.M., 2002. Fabrication of high-density, high aspect ratio, large-area bismuth telluride nanowire arrays by electrodeposition into porous anodic alumina templates. *Advanced Materials* 14 (9), 665-667.
- [24] Schuster, B.E., Wei, Q., Ervin, M.H., Hruszkewycz, S.O., Miller, M.K., Hufnagel, T.C., Ramesh, K.T., 2007. Bulk and microscale compressive properties of a Pd-based metallic glass. *Scripta Materialia* 57 (6), 517-520.
- [25] Simone, A.E., Gibson, L.J., 1998. Effects of solid distribution on the stiffness and strength of metallic foams. *Acta Materialia* 46 (6), 2139-2150.
- [26] Triantafillou, T.C., Zhang, J., Shercliff, T.L., Gibson, L.J., Ashby, M.F., 1989. Failure Surfaces for Cellular Materials under Multiaxial Loads .2. Comparison of Models with Experiment. *International Journal of Mechanical Sciences* 31 (9), 665-678.
- [27] Uchic, M.D., Dimiduk, D.M., Florando, J.N., Nix, W.D., 2004. Sample dimensions influence strength and crystal plasticity. *Science* 305 (5686), 986-989.
- [28] Vajandar, S.K., Xu, D.Y., Markov, D.A., Wikswo, J.P., Hofmeister, W., Li, D.Y., 2007. SiO<sub>2</sub>-coated porous anodic alumina membranes for high flow rate electroosmotic pumping. *Nanotechnology* 18 (27)
- [29] Varghese, O.K., Grimes, C.A., 2003. Metal oxide nanoarchitectures for environmental sensing. *Journal of Nanoscience and Nanotechnology* 3 (4), 277-293.
- [30] Volkert, C.A., Donohue, A., Spaepen, F., 2008. Effect of sample size on deformation in amorphous metals. *Journal of Applied Physics* 103 (8), AN:083539

- [31] Zhang, Y., Li, G.H., Wu, Y.C., Zhang, B., Song, W.H., Zhang, L., 2002. Antimony nanowire arrays fabricated by pulsed electrodeposition in anodic alumina membranes. *Advanced Materials* 14 (17), 1227
- [32] Zheng, M.J., Zhang, L.D., Zhang, X.Y., Zhang, J., Li, G.H., 2001. Fabrication and optical absorption of ordered indium oxide nanowire arrays embedded in anodic alumina membranes. *Chemical Physics Letters* 334 (4-6), 298-302.



**Figures**



**The Anodic Aluminium Oxide (AAO) nano-honeycomb**

Fig.1

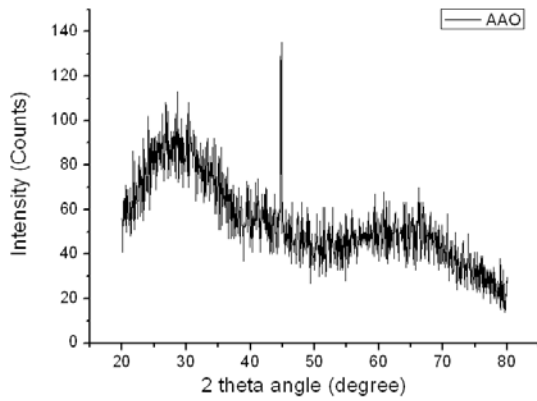


Fig. 2(a)

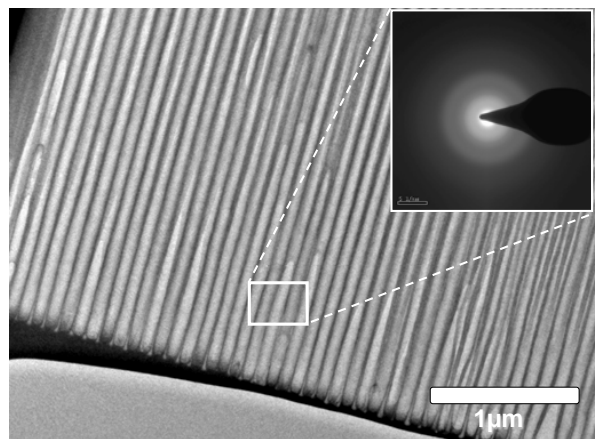


Fig. 2(b)

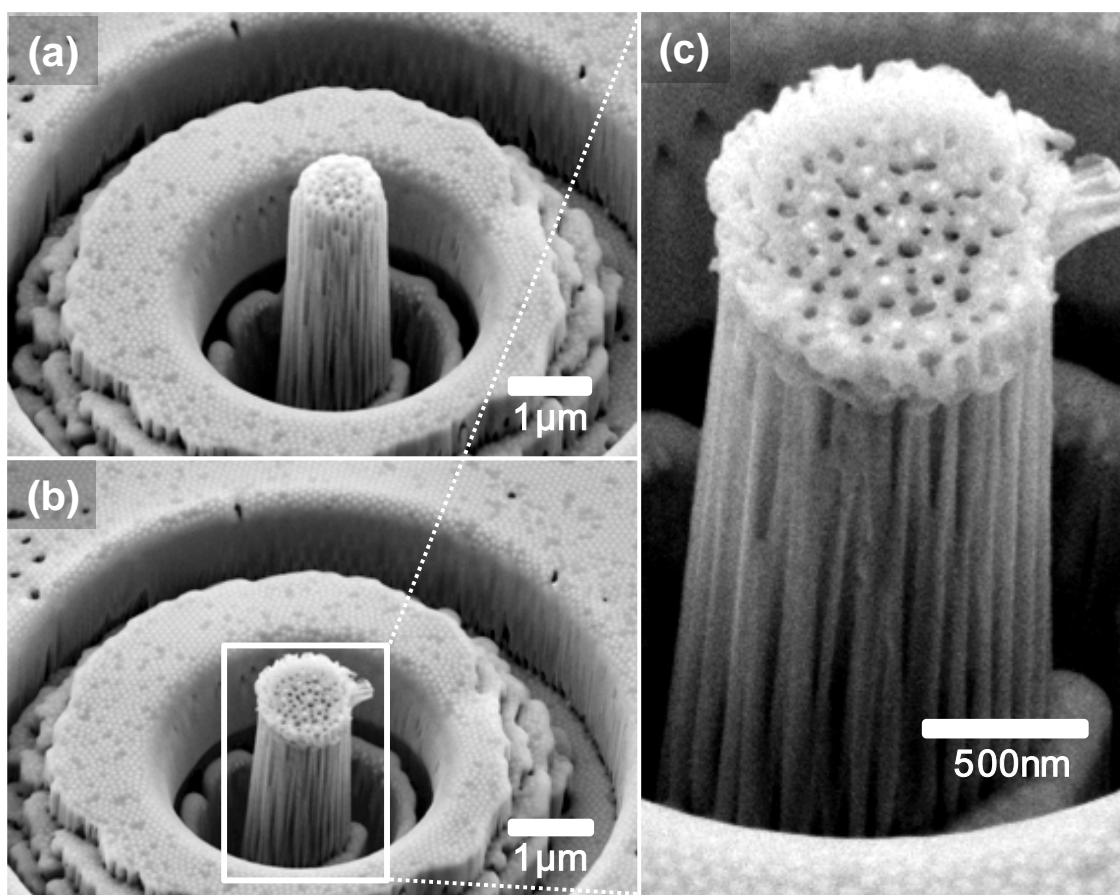


Fig. 3

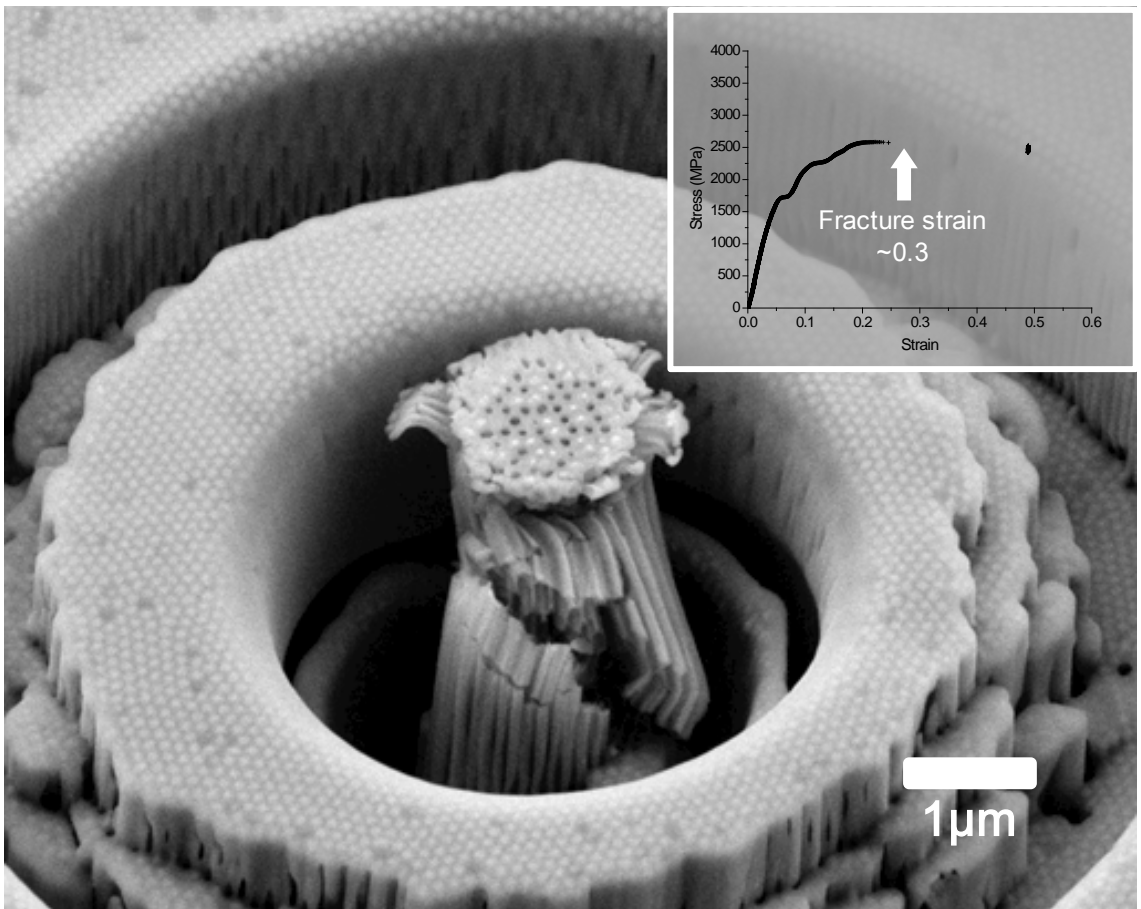


Fig.4

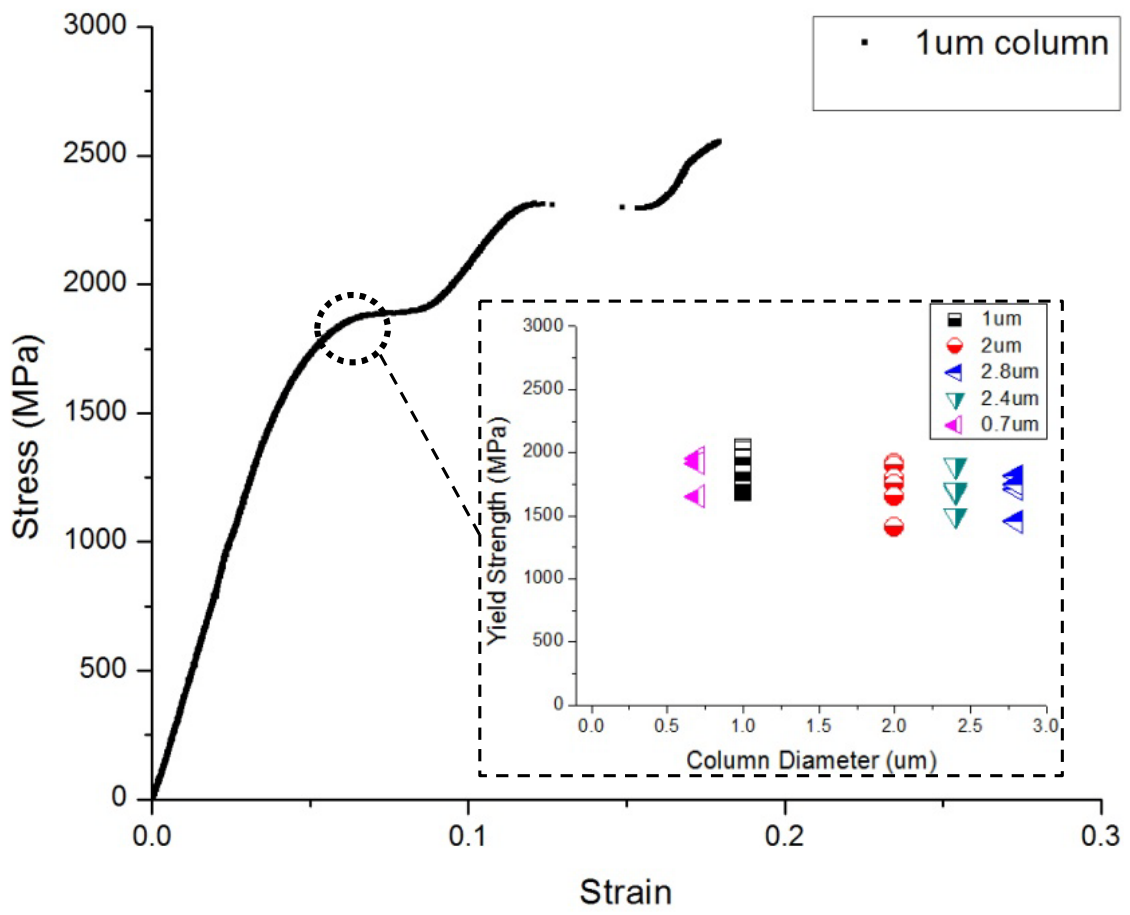


Fig. 5a

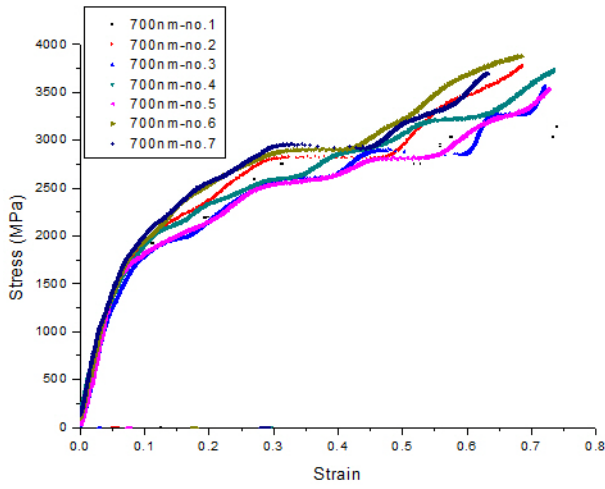


Fig.5b

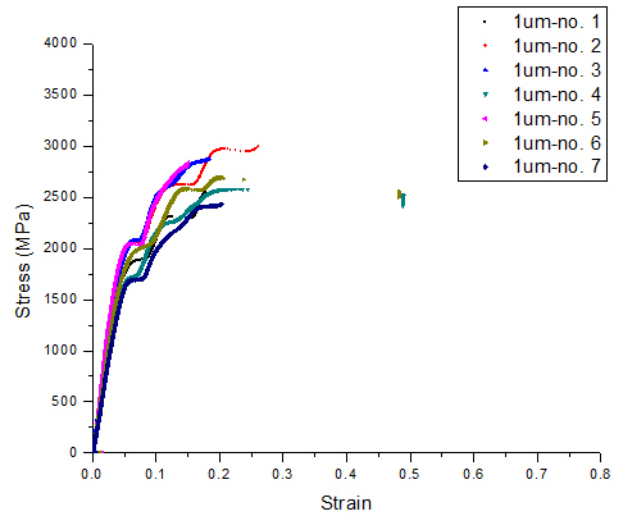


Fig. 5c

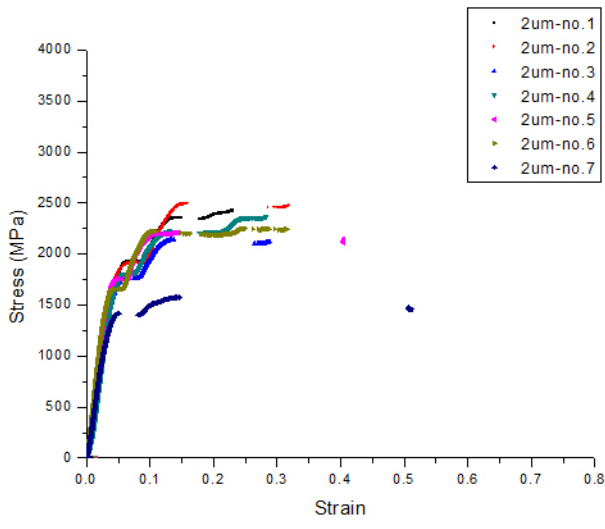


Fig. 5d

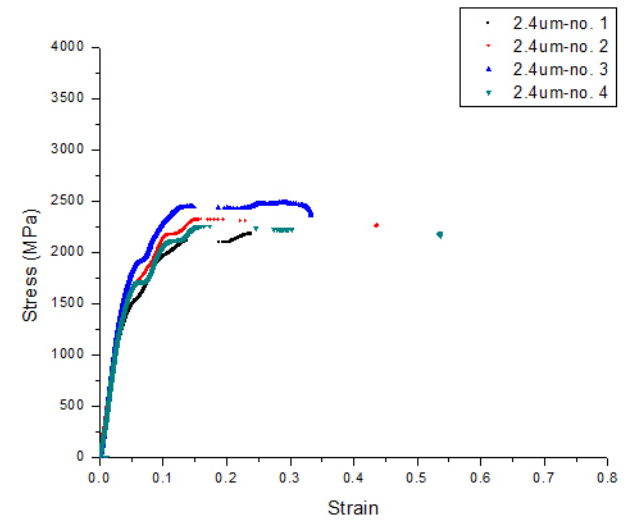


Fig. 5e

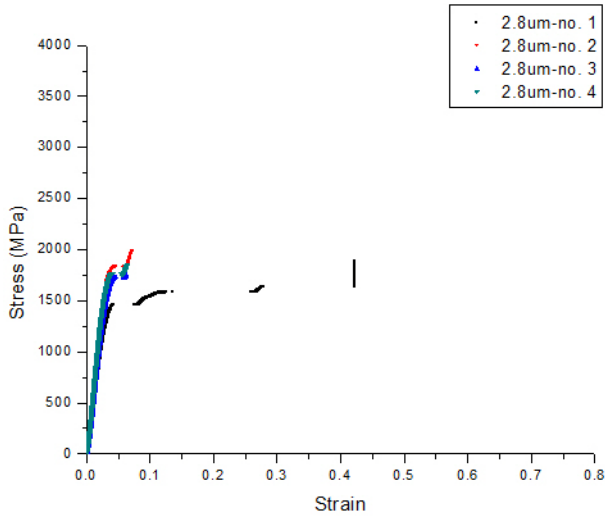


Fig. 5f

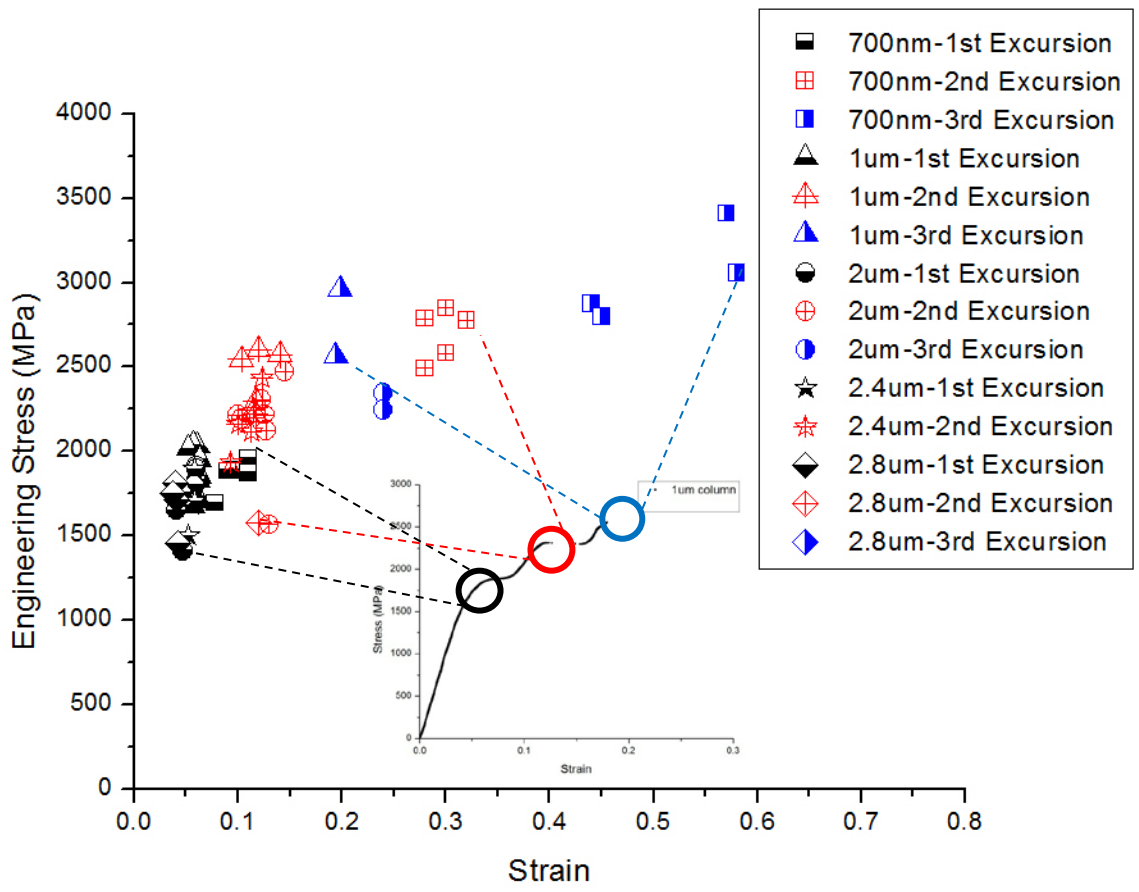


Fig. 6

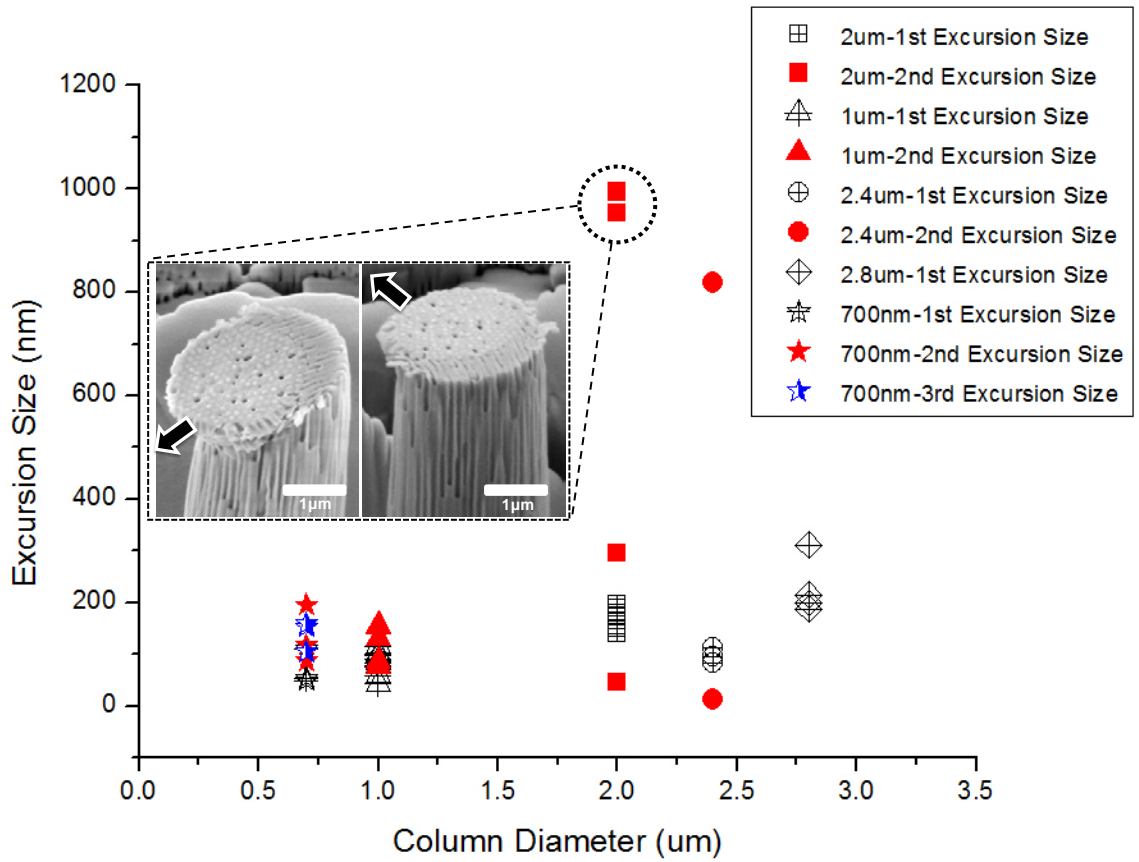


Fig. 7

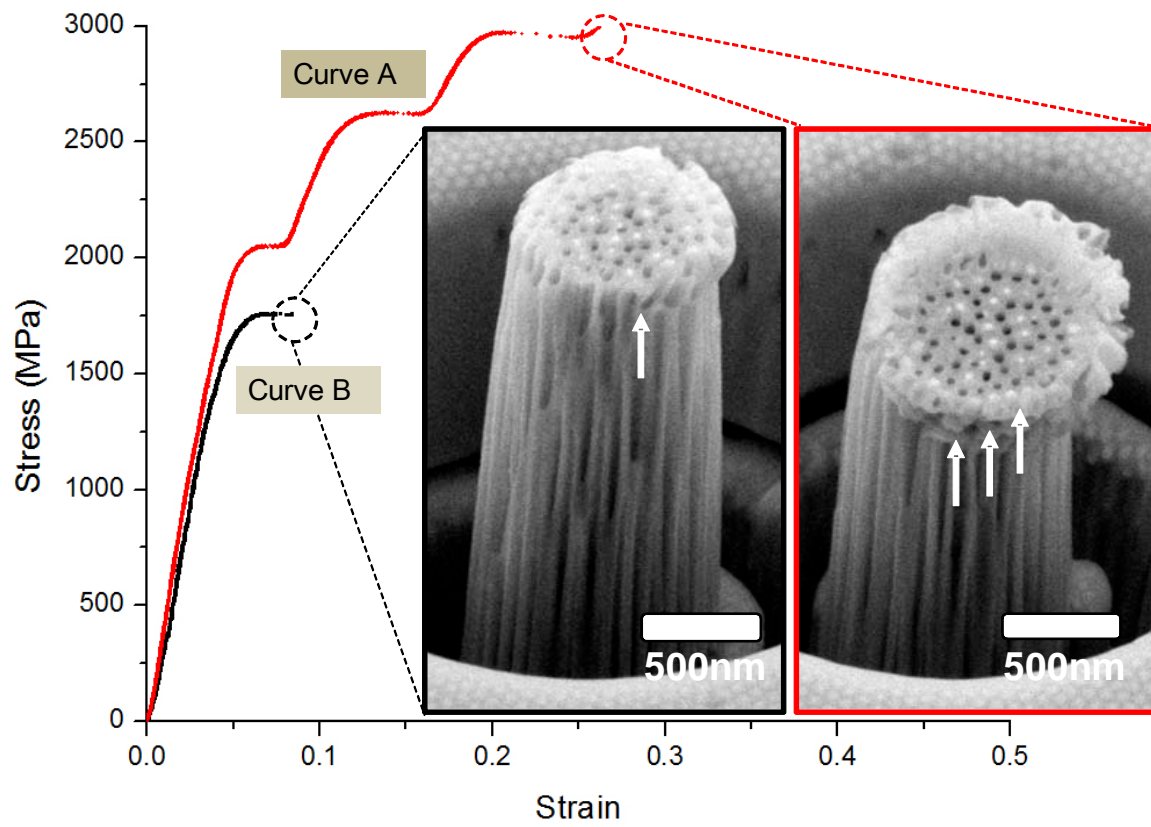


Fig. 8

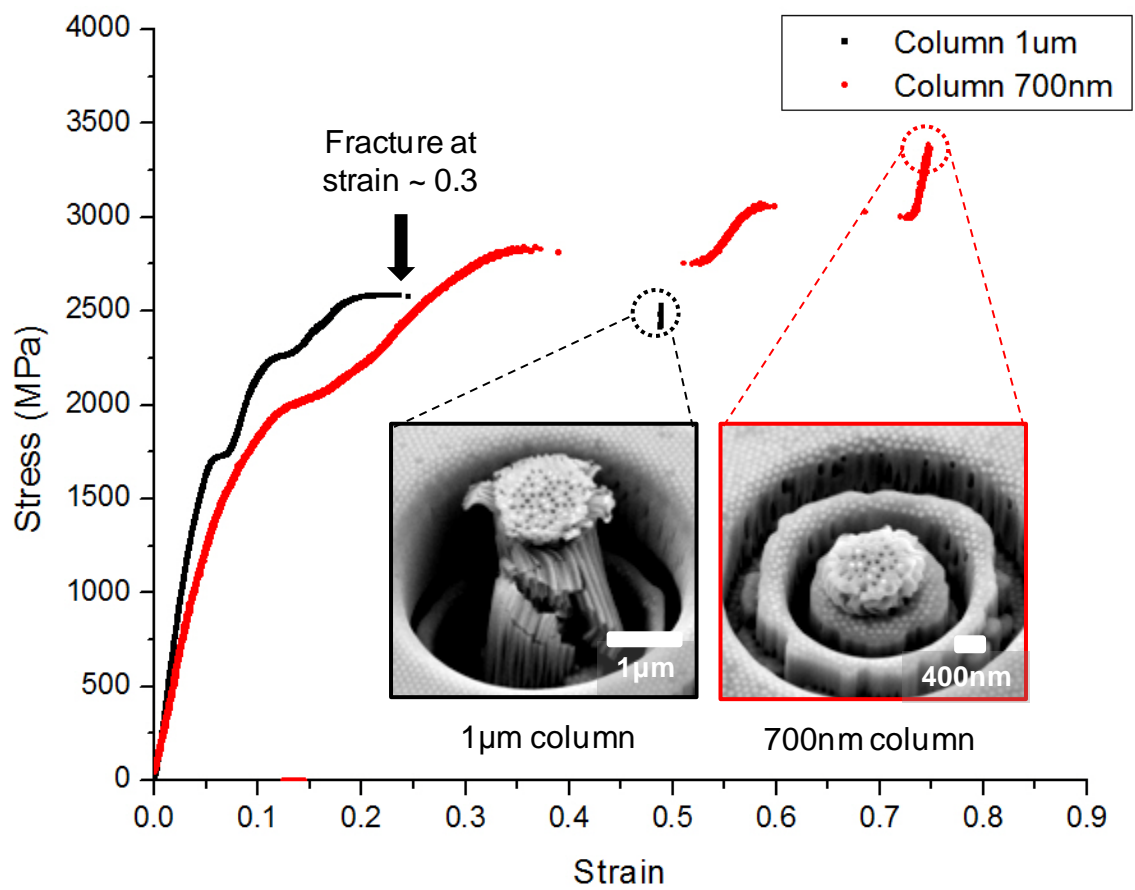


Fig.9  
30

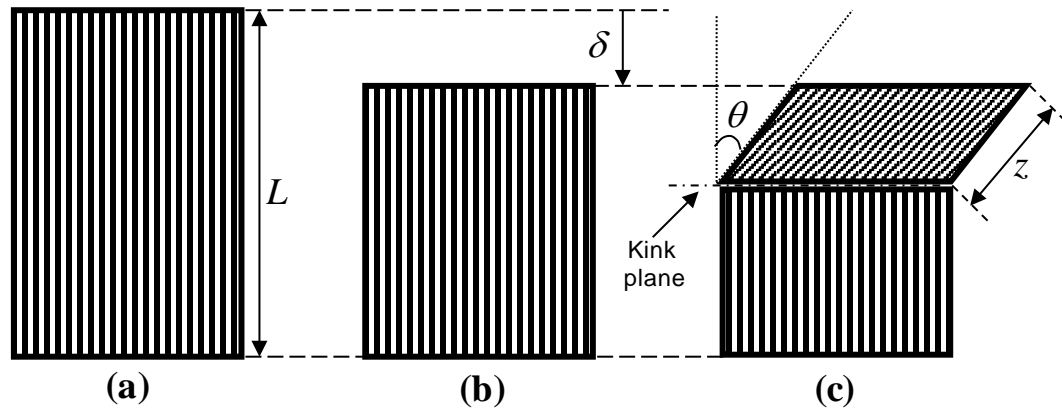


Fig. 10

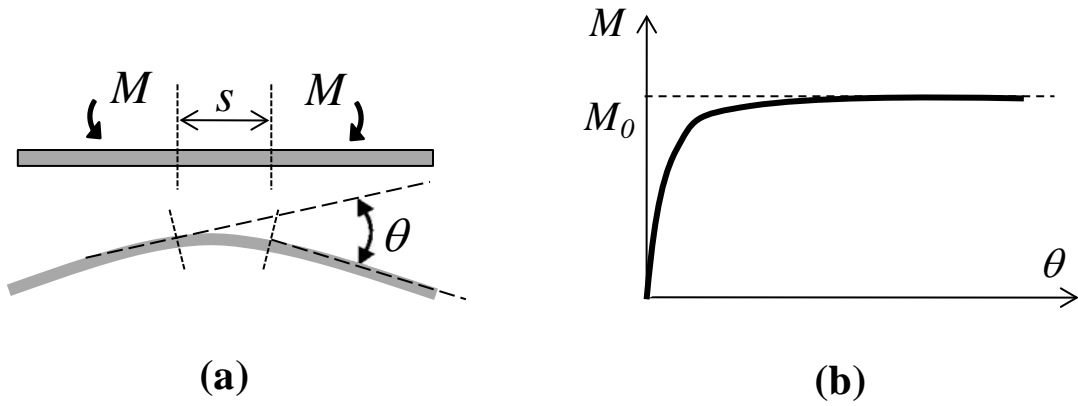


Fig. 11

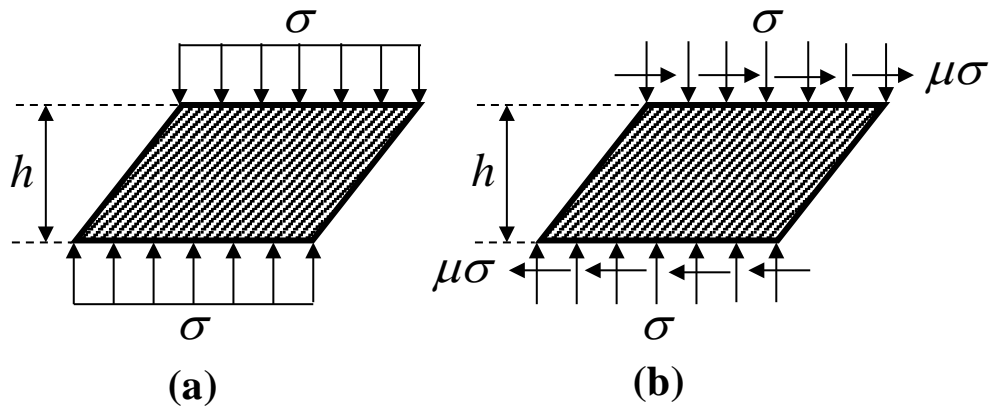


Fig. 12



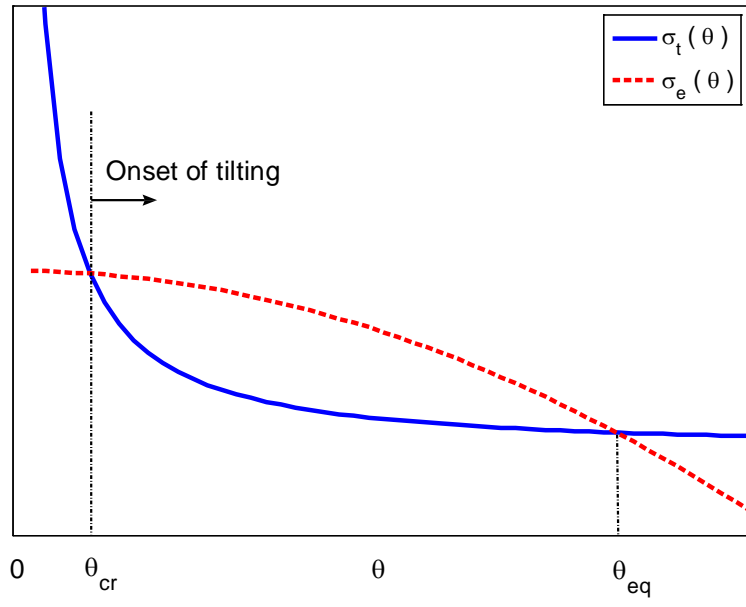


Fig. 13

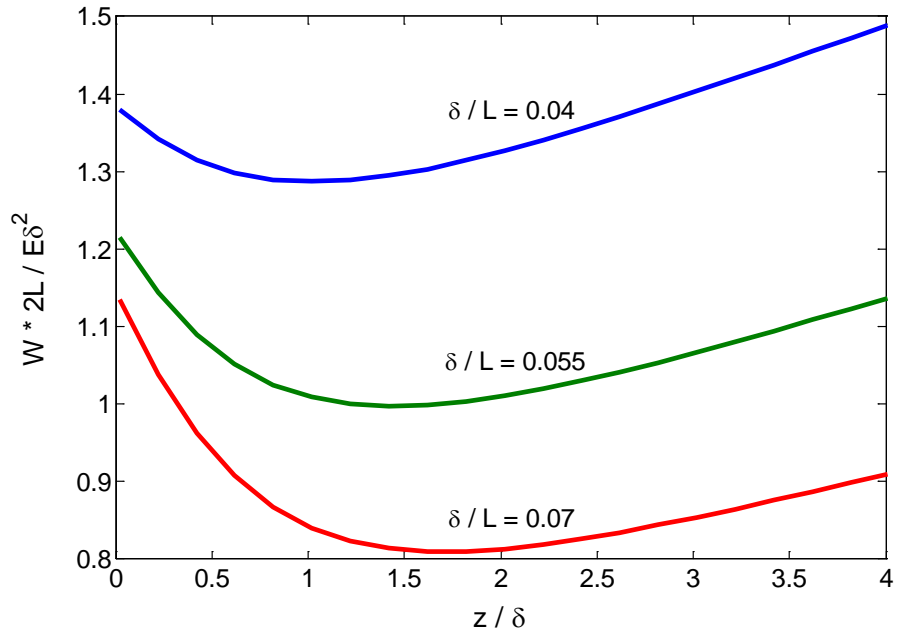


Fig. 14

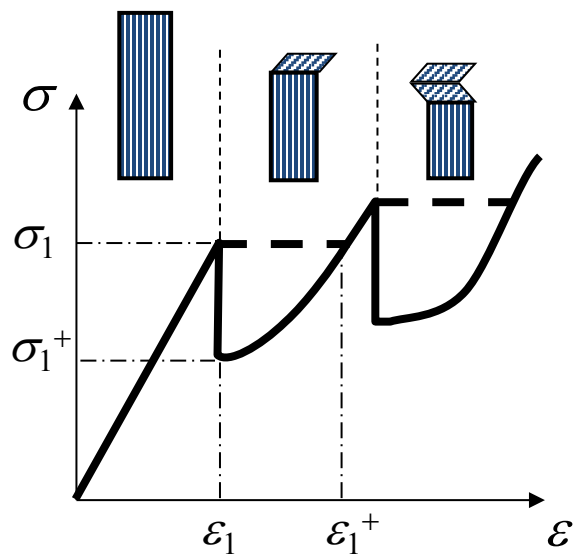


Fig.15

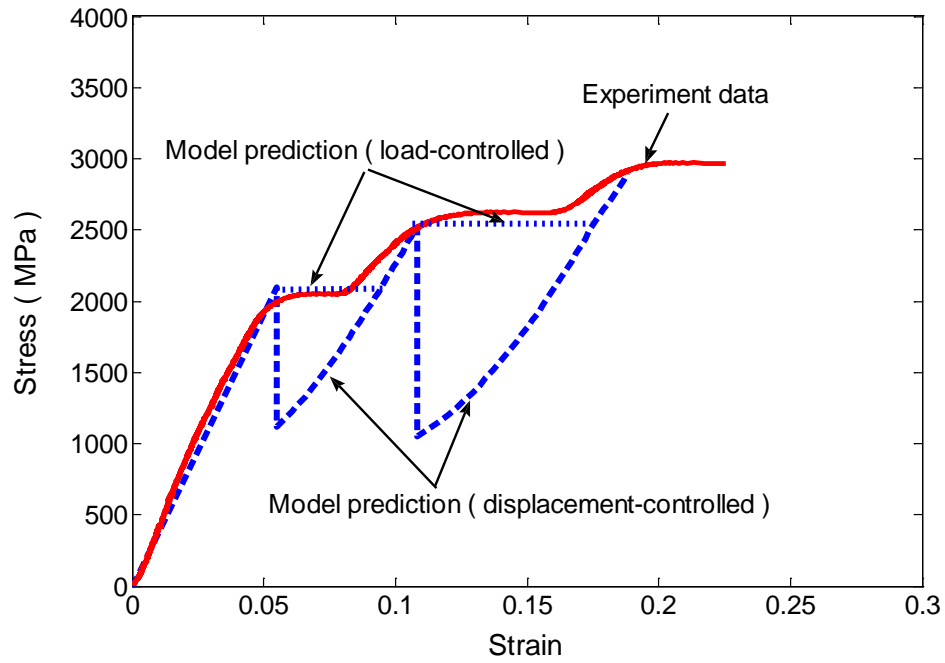


Fig.16

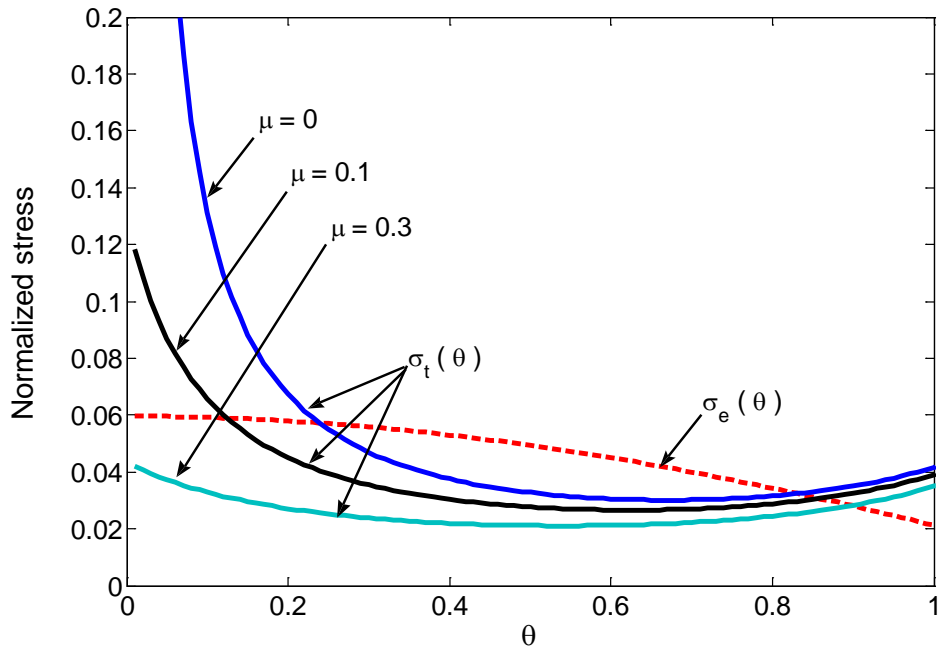


Fig.17